Results in Physics 6 (2016) 217–230

Contents lists available at ScienceDirect

Results in Physics

journal homepage: www.journals.elsevier.com/results-in-physics

Elucidation of the highest valence band and lowest conduction band shifts using XPS for ZnO and $Zn_{0.99}Cu_{0.01}O$ band gap changes

N. Kamarulzaman [a,b,*], M.F. Kasim [a,c], N.F. Chayed [a,c]

[a] Centre for Nanomaterials Research, Institute of Science, Level 3 Block C (Old Engineering Building), Universiti Teknologi MARA, 40450 Shah Alam, Selangor, Malaysia
[b] School of Physics and Materials Studies, Faculty of Applied Sciences, Universiti Teknologi MARA, 40450 Shah Alam, Selangor, Malaysia
[c] School of Chemistry and Environment, Faculty of Applied Sciences, Universiti Teknologi MARA, 40450 Shah Alam, Selangor, Malaysia

ARTICLE INFO

Article history:
Received 7 January 2016
Accepted 3 April 2016
Available online 27 April 2016

Keywords:
Nanomaterials
Rietveld refinement
Doped ZnO
Band gap
Energy band shift

ABSTRACT

ZnO and $Zn_{0.99}Cu_{0.01}O$ nanostructures were prepared by a simple sol–gel method. The band gaps of the materials were systematically studied based on the dependence of the dimensions of the nanostructures as well as the presence of a dopant material, Cu. ZnO and $Zn_{0.99}Cu_{0.01}O$ nanostructures were found to exhibit band gap widening whilst substitution of Cu in the lattice of ZnO caused its band gap to narrow with respect to the pure ZnO materials. In order to understand the phenomenon of band gap change, structural, spectroscopic, particle size and morphological studies were done. The band gap change occurring when the materials were in the nanostructured phase was proven to be mainly due to the downward shift of the valence band. Interestingly, when the band gaps of the pure ZnO and Cu doped ZnO were compared, the band gap changes were due to different shifts of the valence bands.

Introduction

ZnO is a very interesting material to study due to its unique physical and chemical properties resulting in applications such as blue and ultra-violet optical devices, sensors, solar cells and other new nanotechnology based devices [1–5]. ZnO is said to have a direct band gap of 3.37 eV [1–4] but this value has been found not to be unique and lately, using more accurate modern instruments, the values have been revised to between 3.1 and 3.4 eV [2,6]. Thus, the band gap of ZnO is found to be sensitive to the route of synthesis and preparation conditions as well as its physical dimensions. The band gap of ZnO can be changed by either decreasing the size of the crystallites [2,7–9] or by doping [10–12]. There are two types of doping of which the first is when a foreign ion replaces a host cation or anion in its position in the crystal lattice site and the second type is when the foreign ion is placed in the interstices of the crystal structure. Substitutional doping can be done by a chemical reaction method that forces the dopant element to be introduced into the crystal lattice sites of the material [10,11]. If the dopant is a cation, it will replace the host cation site and if the dopant is an anion, it will likewise replace the anion at its particular site in the crystal lattice. Single phase materials that are isostructural to the initial material will be produced. However, these new compounds will exhibit novel characteristics which will be useful for future applications.

Much work on ZnO doping has been done [13–20]. Doping can cause either an increase or decrease of band gaps. As an example, according to Shan et al. Cd doping in ZnO causes the band gap of the material to decrease while Mg doping in ZnO causes it to increase [15]. Therefore, band gap tuning via dopant materials is quite possible. Several synthesis methods such as hydrothermal [1], combustion [21], spray pyrolysis [22], sol–gel [19], etc. have been employed to produce ZnO. Among these techniques, catalysts are used [23,24] contaminating the final products. In this work, the ZnO and Cu doped ZnO materials are synthesized without using any catalysts, thus, simplifying the synthesis route and ensuring purity to a high degree. Since this work investigates the band gaps and changes in band gap of materials, and band gaps are very sensitive to the presence of impurities and multi phases [25], it is very important that the final product must be single phase and pure. Contributions from other minor phases or impurities are detrimental to the experimental results because band gaps are affected by minor presence of impurities or the presence of other phases.

Although much work has been published on ZnO and ZnO doped materials [14–25], there are still many unresolved issues on this subject. As an example, there are no clear explanations of the band gap widening of nanostructured ZnO in the literature

* Corresponding author at: Centre for Nanomaterials Research, Institute of Science, Level 3 Block C (Old Engineering Building), Universiti Teknologi MARA, 40450 Shah Alam, Selangor, Malaysia. Fax: +60 3 55443870.
E-mail addresses: norlyk@salam.uitm.edu.my, norly003@yahoo.co.uk (N. Kamarulzaman).

http://dx.doi.org/10.1016/j.rinp.2016.04.001
2211-3797/

Table 1
Sample ID for ZnO and $Zn_{0.99}Cu_{0.01}O$ annealed at various temperatures for 24 h.

Samples	Annealing temperature (°C)	Sample ID
ZnO	400	Z400
	500	Z500
	600	Z600
	700	Z700
	800	Z800
	1200	Z1200
$Zn_{0.99}Cu_{0.01}O$	400	ZC400
	500	ZC500
	600	ZC600
	700	ZC700
	800	ZC800
	1200	ZC1200

beyond the presence of vacancies [26,27] but with no experimental proofs of the existence of the vacancies given. For Cu doped materials, it is very difficult to force Cu into the lattice of ZnO producing pure powders. For our $Zn_{1-x}Cu_xO$, we can only manage a Cu content of $x = 0.01$. Yan et al. [25] and Chow et al. [28] said that they have produced $Zn_{(1-x)}Cu_xO$, with $x = 0.03$ but since no XRD results were shown by Yan, and low intensity XRD results showing the presence of Cl_2 (albeit, it was not explained how Cl_2 can produce a peak in an XRD pattern!) was shown by Chow, it has not been established if the samples are really pure or of single phase. Thus, it is hard to say if the observed band gap change was due to the impurities, multiphases or the materials themselves. In addition, no energy dispersive X-ray spectroscopy (EDS) or equivalent methods in the work have been shown to prove that a substitution of

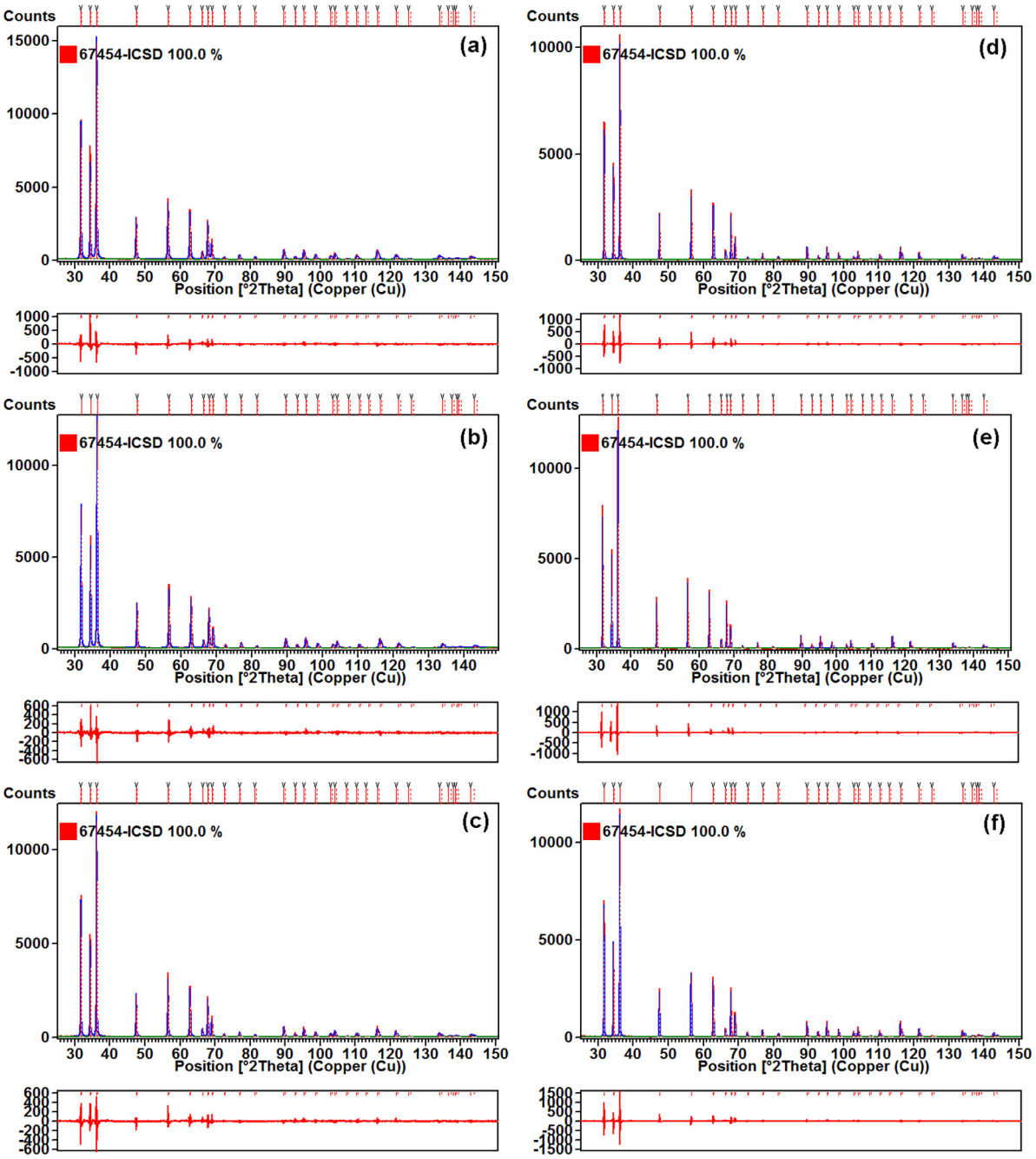

Fig. 1. Rietveld refinements of XRD patterns for (a) Z400 (b) Z500 (c) Z600 (d) Z700 (e) Z800 (f) Z1200 samples.

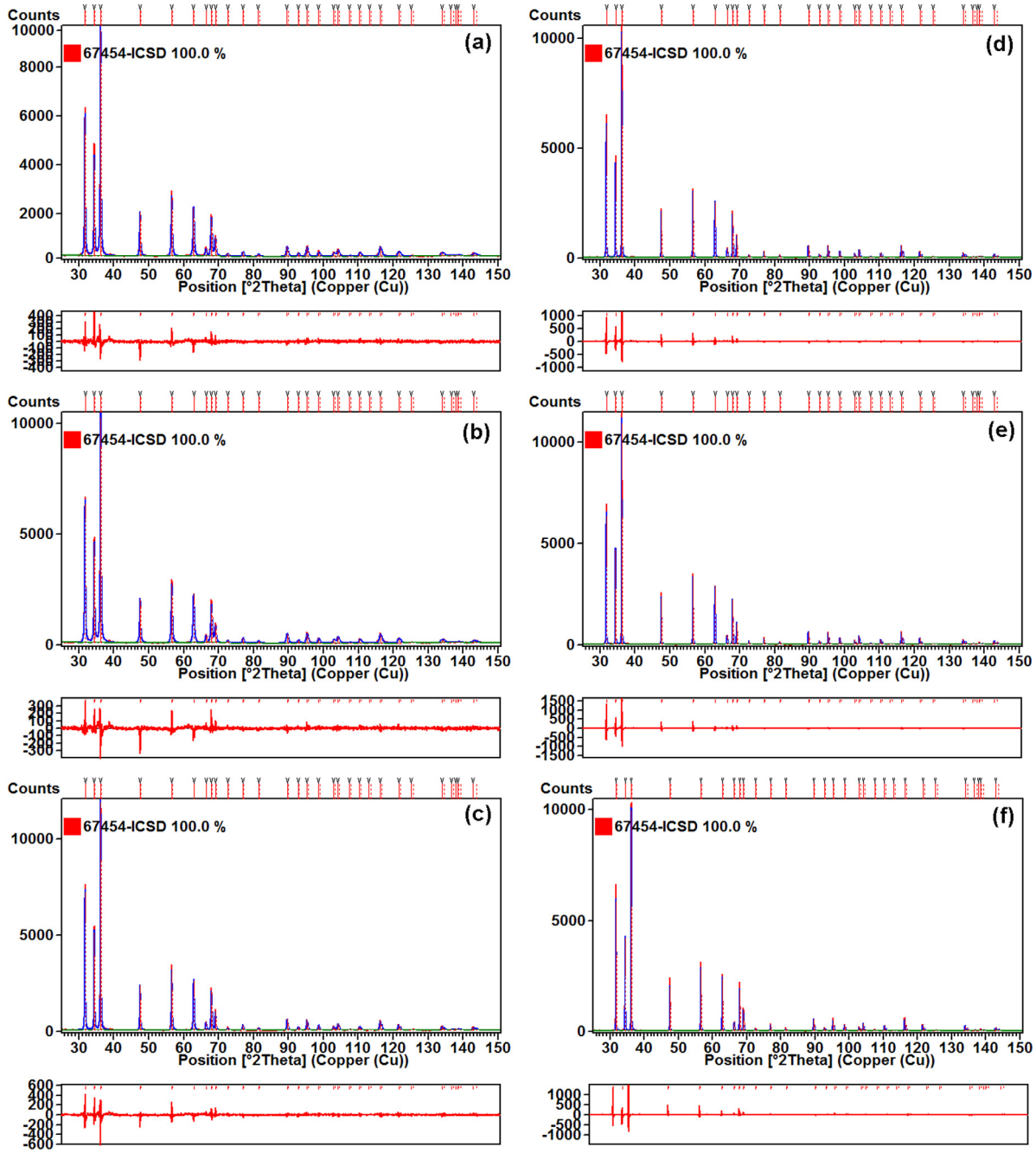

Fig. 2. Rietveld refinements of XRD patterns for (a) ZC400 (b) ZC500 (c) ZC600 (d) ZC700 (e) ZC800 (f) ZC1200 samples.

Table 2
Crystallographic parameters of the ZnO samples extracted from the Rietveld refinements of the XRD data sets (s.o.f. = site occupancy factor).

Temperature (°C)	$a = b$ (Å)	c (Å)	V (Å^3)	c/a	Rw	χ^2	s.o.f. of Zn	s.o.f. of O
400	3.2496	5.2058	47.607	1.602	8.1	1.6	0.95	1.00
500	3.2498	5.2061	47.617	1.602	8.7	1.4	0.96	1.00
600	3.2497	5.2058	47.610	1.602	9.9	1.4	0.95	1.00
700	3.2498	5.2053	47.608	1.602	12.7	1.7	0.95	1.00
800	3.2505	5.2053	47.630	1.601	13.6	1.9	0.95	1.00
1200	3.2496	5.2032	47.583	1.601	12.3	1.9	0.97	1.00

Table 3
Crystallographic parameters of the $Zn_{0.99}Cu_{0.01}O$ samples extracted from the Rietveld refinements of the XRD datasets (s.o.f. = site occupancy factor) and Zn and Cu values obtained from EDX.

Temperature (°C)	$a = b$ (Å)	c (Å)	V (Å^3)	c/a	Rw	χ^2	s.o.f. of Zn + Cu	s.o.f. of O	EDX (%)	
									Zn	Cu
400	3.2494	5.2060	47.603	1.602	7.9	1.33	0.95	1.00	99.02	0.98
500	3.2496	5.2059	47.609	1.602	7.4	1.34	0.95	1.00	99.03	0.97
600	3.2499	5.2050	47.608	1.602	8.6	1.38	0.97	1.00	98.96	1.04
700	3.2502	5.2042	47.612	1.601	12.8	1.66	0.96	1.00	99.02	0.98
800	3.2502	5.2043	47.610	1.601	13.6	1.84	0.97	1.00	99.02	0.98
1200	3.2502	5.2050	47.617	1.601	13.9	1.80	0.97	1.00	98.99	1.01

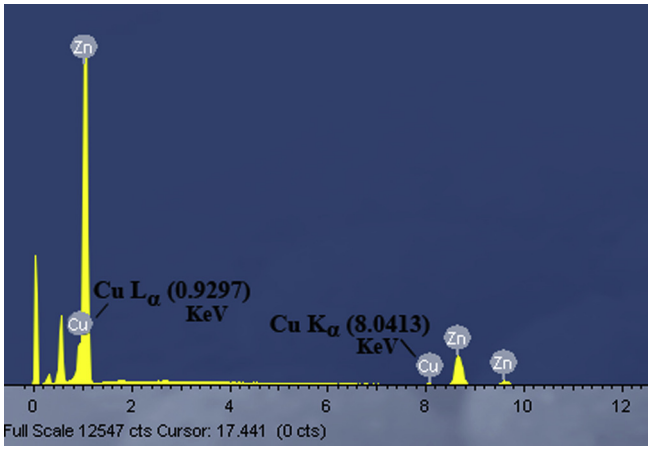

Fig. 3. EDS spectrum for ZC1200 samples.

$x = 0.03$ has been realized. Liu et al. [19] also said that they have achieved $x = 0.03$ in $Zn_{(1-x)}Cu_xO$ material but similarly, no proofs such as EDS data were shown. In the Cu doping, most scientists presented work on $Zn_{1-x}Cu_xO$ thin films [29–31] instead of bulk powders and in thin films, it is hard to establish if substitutional or interstitial doping has been achieved because the XRD data are of low counts and the structural parameters are hard to determine. In most cases, no EDS (or equivalent) results were done to prove that indeed the particular percentage of Cu substitution has been achieved. In band gap studies, band gap narrowing has been observed in the Cu doped material but no satisfactory explanations have been put forward as to the mechanism responsible for this observed phenomenon. To really explain the phenomenon, one must first of all establish if the Cu doping was substitutional or interstitial or whether the sample is made up of the double phases of ZnO and CuO. In published literature, it is also not established if the valence band (VB) shift is due to the Cu^+ or Cu^{2+} ions in the samples. There is much speculation of what contributes to band gap widening in nanomaterials but there is a lack of experimental proof to the explanations put forward. This work addresses these issues and attempts to prove and explain band gap narrowing in nano structured and Cu doped ZnO materials.

Experimental

The synthesis of ZnO and Cu substituted ZnO powders was prepared using a simple sol–gel method. The starting materials used were zinc acetate dehydrate (R & M chemicals, 99.5% purity) and copper (II) acetate monohydrate (Riedel-de Haen, 99% purity). These materials were first dissolved in absolute ethanol and stirred for about 1 h. The pH of the solution was 5.2 and no catalyst was used in the synthesis method. The materials were slow dried and

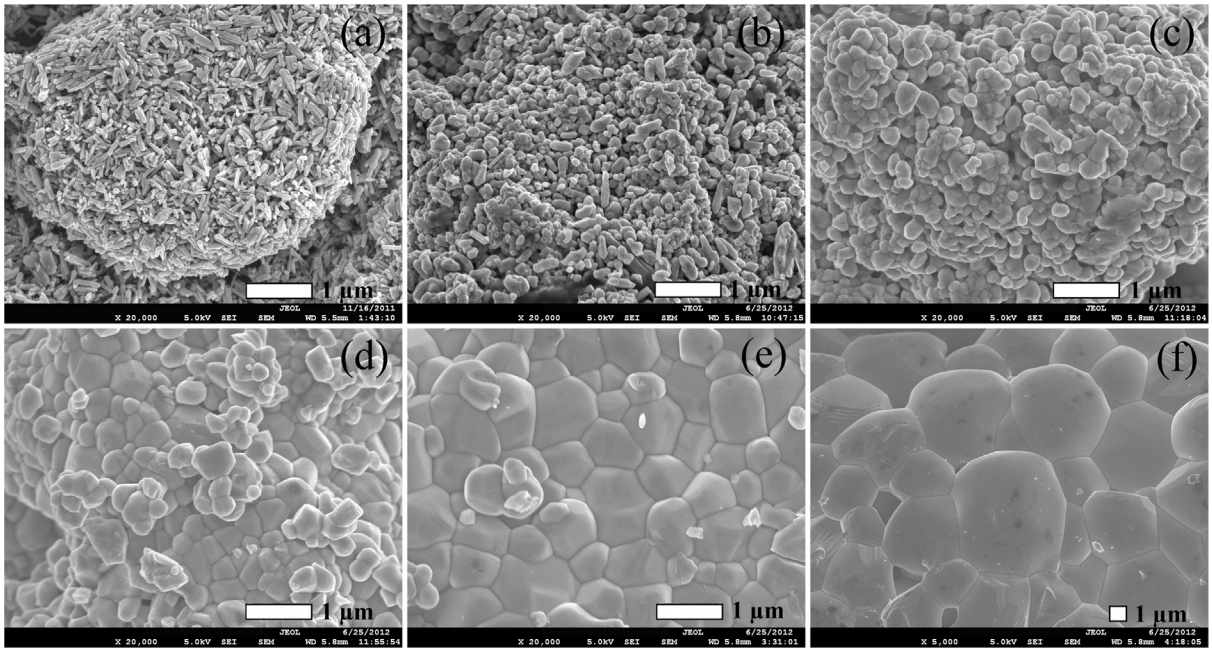

Fig. 4. SEM images of (a) Z400 (b) Z500 (c) Z600 (d) Z700 (e) Z800 (f) Z1200 samples.

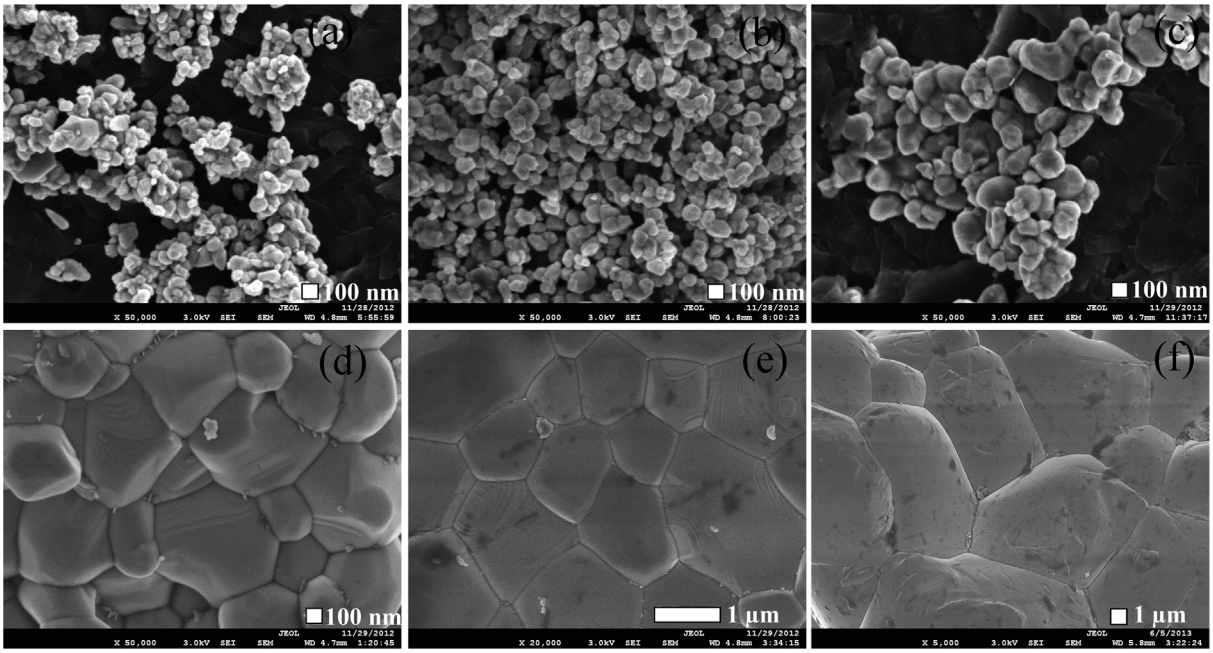

Fig. 5. SEM images of (a) ZC400 (b) ZC500 (c) ZC600 (d) ZC700 (e) ZC800 (f) ZC1200 samples.

Table 4
The average length, diameter and aspect ratios for ZnO and $Zn_{0.99}Cu_{0.01}O$ materials.

Temperature (°C)	Sample	Average length (nm)	Average diameter (nm)	Aspect ratio
400	ZnO	320.37	90.5	3.54
	$Zn_{0.99}Cu_{0.01}O$	155.02	75.62	2.05
500	ZnO	381.10	128.75	2.96
	$Zn_{0.99}Cu_{0.01}O$	103.2	80.00	1.29
600	ZnO	316.71	229.5	1.38
	$Zn_{0.99}Cu_{0.01}O$	227.50	186.47	1.22
700	ZnO	481.46	379.1	1.27
	$Zn_{0.99}Cu_{0.01}O$	589.24	495.16	1.19
800	ZnO	625.95	504.80	1.24
	$Zn_{0.99}Cu_{0.01}O$	1207.5	1050.00	1.15
1200	ZnO	5224.27	4706.55	1.11
	$Zn_{0.99}Cu_{0.01}O$	9472.83	8027.82	1.18

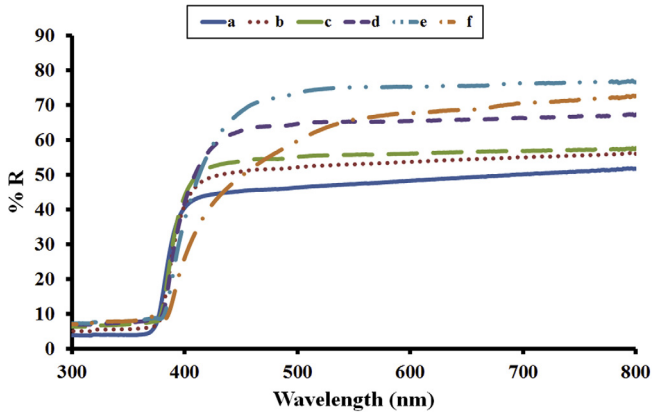

Fig. 7. UV–Vis spectroscopic results of (a) Z400 (b) Z500 (c) Z600 (d) Z700 (e) Z800 (f) Z1200 samples.

grey precursors were obtained. The precursors were then grounded using an agate mortar to obtain fine powders of ZnO and $Zn_{0.99}Cu_{0.01}O$. Thermal studies were done using a Simultaneous Thermogravimetric Analyzer (STA), SETARAM SETSYS Evolution 175. This equipment can measure the Thermogravimetric Analysis (TGA) and Differential Scanning Calorimetry (DSC) graphs simultaneously. Based on the TG/DSC, the precursors were annealed at five different temperatures of 400, 500, 600, 700, 800 and 1200 °C for 24 h. Structural studies on the annealed samples were done using X-ray Diffraction (XRD) and the PANalytical X'pert Pro MPD diffractometer with a solid state detector (Accelerator) was used. The XRD measurements were done using a Bragg–Brentano optical configuration in ambient conditions with the spinning mode to

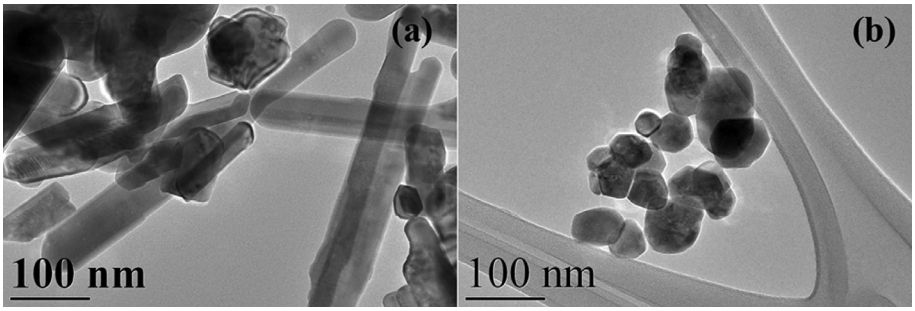

Fig. 6. TEM images for (a) Z400 and (b) ZC400 samples showing nano structured rod-like and spherical shaped crystals respectively.

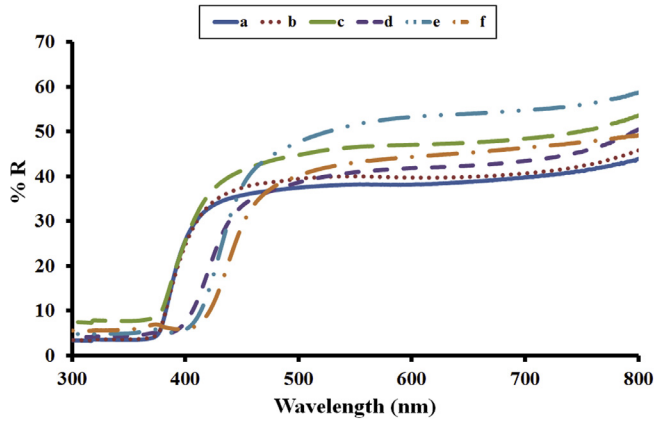

Fig. 8. The UV–Vis spectroscopic results of (a) ZC400 (b) ZC500 (c) ZC600 (d) ZC700 (e) ZC800 (f) ZC1200 samples.

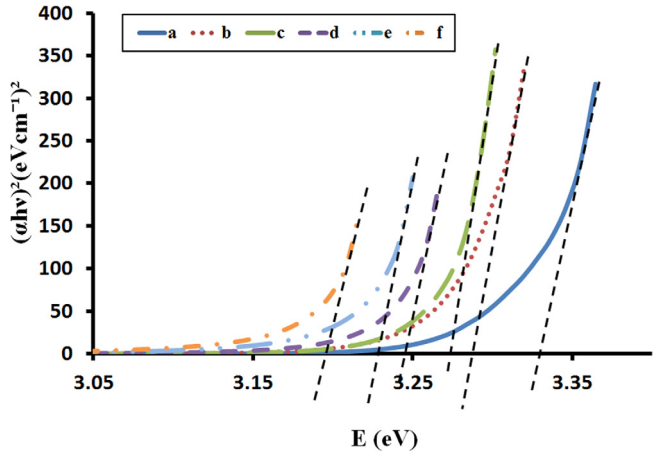

Fig. 9. Tauc plots of (a) Z400 (b) Z500 (c) Z600 (d) Z700 (e) Z800 (f) Z1200 samples.

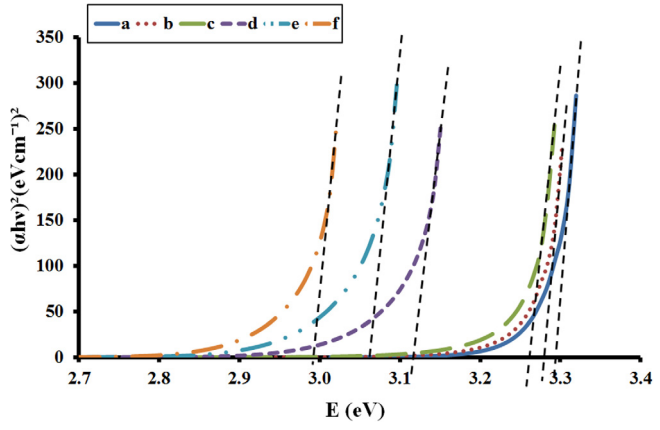

Fig. 10. Tauc plots of (a) ZC400 (b) ZC500 (c) ZC600 (d) ZC700 (e) ZC800 (f) ZC1200 samples.

reduce effects of preferred orientation. The X-ray beam used was the CuK_{α} radiation. High quality datasets were obtained with the highest peak around 10,000 counts as statistically required for proper quantitative XRD analysis [32–34]. Rietveld refinements of the XRD patterns for ZnO and $Zn_{0.99}Cu_{0.01}O$ materials were done using the PanAlytical X'pert Highscore Plus software. The refinements were executed with the ICSD 67454 (hexagonal crystal structure with space group P63mc) as the structural reference.

Table 5
Band gap energies of ZnO and $Zn_{0.99}Cu_{0.01}O$.

Temperature (°C)	ZnO	$Zn_{0.99}Cu_{0.01}O$
400	3.328	3.280
500	3.290	3.270
600	3.275	3.260
700	3.245	3.180
800	3.230	3.020
1200	3.190	2.980

The morphology and crystallite size of the materials were examined using Field Emission Scanning Electron Microscopy (FESEM-JEOL JSM-7600F). The dopant content is measured using an EDS (the Oxford INCA X-Max 51-XMX 0021). For the nanostructured ZnO and $Zn_{0.99}Cu_{0.01}O$ samples, the small crystal size is further illustrated using a High Resolution Transmission Electron Microscopy (HRTEM), the JEOL JEM-2100F to give better resolution and clearer information of the morphology and dimensions of the nanostructures.

The light absorption properties of the materials were studied using a UV–Visible spectrophotometer, the Perkin Elmer Lambda 950 UV–Vis-NIR. The measurements were done in reflection mode using the reduced reflectance technique in ambient conditions. The oxidation states, chemical environment and valence band studies of the materials were done by X-ray photoelectron spectroscopy (XPS) using the JEOL JPS-9200 photoelectron spectrometer. The XPS spectra were recorded using a monochromator and Al K_{α} (1486 eV) radiation as the X-ray source. A charge neutralizer was used to reduce charging effects and data were taken using a pass energy of 10 eV. The samples used were pelletized and prior to insertion into the measuring chamber, were heated at 100 °C to minimize the presence of hydrocarbons on the surface of the materials.

Results and discussions

Sample identifications (IDs) for ZnO and Cu doped ZnO are listed in Table 1. The refined XRD results of the materials are shown in Figs. 1 and 2 of all the samples for ZnO and the Cu doped $Zn_{0.99}Cu_{0.01}O$ materials. Tables 2 and 3 shows the crystallographic parameters extracted from the Rietveld refinements of XRD datasets for ZnO and $Zn_{0.99}Cu_{0.01}O$ samples respectively. The XRD data analysis shows that all samples are of pure hexagonal phase materials. No impurity peaks are observed in the high quality patterns. The lattice parameters of the ZnO materials agree well with published data [16]. It is observed that the cell volume for the Z400 sample is smaller and the cell volume from the Z500 sample onwards tend to decrease, except for the Z800 sample. The Z400 sample has a smaller cell volume believed to be due to the morphology of the nanocrystals which is rod-like in shape as discussed later in the SEM results. Starting from the Z500 sample, the morphology of the samples begin to change to more spherical shapes and generally, there is a decrease in the lattice parameters for the ZnO materials with the increase of temperature, except for the Z800 sample. It is believed that the Z800 sample did not follow the normal trend because of the inhomogeneity of the crystallite size and mixture of morphologies. It is observed that for ZnO samples, the c/a value shows a steady decrease as the annealing temperature increases implying that there is contraction in the [002] direction of the crystallographic plane as crystallinity increases. The decrease of the c/a value with the increase of temperature implies that the packing density along this c-axis increases as the crystallite size increases. The oxygen site occupancies are all full but the cation 2b site contains a small amount of vacancies. Contrary to general belief, XRD quantitative results

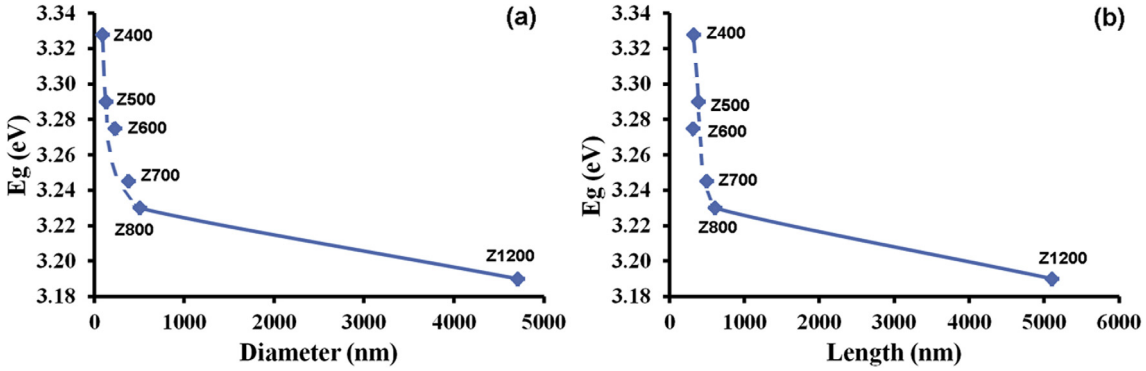

Fig. 11. The graph of (a) band gap energies (Eg) against diameter and (b) band gap energies (Eg) against length for ZnO materials.

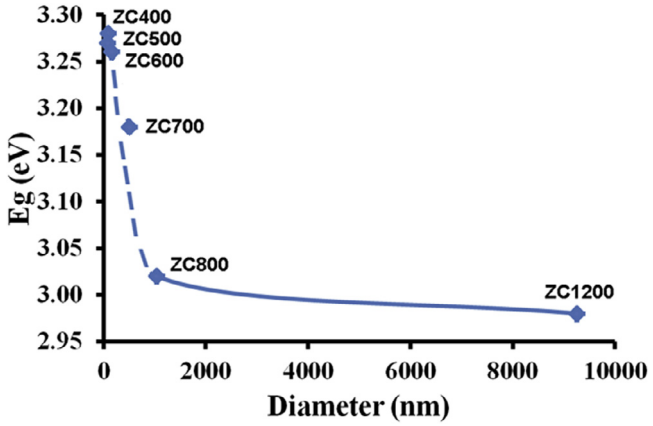

Fig. 12. The graph of band gap energies (Eg) against diameter for $Zn_{0.99}Cu_{0.01}O$ materials.

show that there are no oxygen vacancies in the ZnO materials [25,35,36]. Since it is well known that Zn exhibit a strong affinity to oxygen, and oxygen is easily available, the full site occupancies for oxygen is supportive of this fact. Conversely, for $Zn_{0.99}Cu_{0.01}O$ materials, the cell volume seems to generally increase with increasing annealing temperature. This is different from the observed cell volume results of the ZnO materials. However, the *c*/*a* of the Cu doped compounds generally also decreases with the increase of annealing temperature agreeing with the *c*/*a* results of the pure ZnO materials. Implications to the Cu doped samples are that even though the cell volume increases with temperature, the packing density still decreases suggesting that similar to the ZnO case, a more compact atomic packing along the *c*-axis direction occurs as the annealing temperature increases. There are vacancies observed at the metal site occupancies and no vacancies at the oxygen site. It is observed that there is no cation or anion disorder in the materials suggesting that antisites are not present in these materials, as believed by some researchers [37–39]. From the point of view of crystal structure, it is not probable that anions occupy cation sites and vice versa for stable materials such as ZnO in the hexagonal phase because they are what is called "special positions" in crystallography and the structure will be unstable if this were to occur. Furthermore, it upsets the symmetry of the crystal. Thus, we strongly disagree with the comments of the researchers regarding the antisite explanations.

The absence of impurity peaks implies that the Cu ions have been successfully introduced into the ZnO lattice. The Cu^{2+} ions have slightly lower ionic radius in tetrahedral coordination compared to the Zn^{2+} ions (Zn^{2+} ionic radius = 0.60 Å, Cu^{+} ionic radius = 0.60 Å; and Cu^{2+} ionic radius = 0.57 Å for coordination number = 4 [40]) making it an ideal element, size wise, for the substitutional doping of Cu in the ZnO crystal structure. In addition, the stable oxidation state of Cu is +2 which is similar to the stable oxidation state of Zn which is also +2. The cell volume of the $Zn_{0.99}Cu_{0.01}O$ is found to be generally smaller than that of the pure ZnO sample as expected because of the presence of the smaller copper ions (Cu^{2+}) in the crystal lattice. The exception is for samples ZC700 and ZC1200 and this is believed to be due to the influence of the crystallite size and morphology. Thus, it can be said that the decrease in cell parameters of the doped materials with respect to the pure ZnO at the same temperature is attributable to the presence of the smaller Cu^{2+} ions in the $Zn_{0.99}Cu_{0.01}O$ lattice. Fig. 3 shows the spectrum of the ZC1200 of the Cu doped sample. The spectrum clearly shows the presence of the Cu in the sample and the quantification is given in Table 3. It shows that the Zn–Cu content in the doped samples is very close to the calculated synthesized values. Therefore, from both XRD and EDS results, it can be concluded that the substitutional doping of Cu in the ZnO lattice has been successfully achieved.

Examination of crystallite size via SEM reveals that size and morphology of low and high temperature annealed samples are very different. The SEM images of the ZnO samples in Fig. 4 show that nanostructured ZnO is obtained at annealing temperatures of 400–700 °C. At the lower temperatures of between 400 and 500 °C, the morphology of the crystals is short nano rods with the 400 °C sample showing more pronounced rod-like shapes. The morphology becomes more spherical at higher temperatures. This is different for the $Zn_{0.99}Cu_{0.01}O$ materials as shown in Fig. 5 which do not show many rod-like shapes for the 400 and 500 °C samples except for an isolated few particles. The dimensions of the crystallites are still in the nano range at lower annealing temperatures. The general shape of the particles is spherical unlike those of the ZnO materials at these temperatures which are rod-like in shape. The small crystallite size of the low temperature annealed samples is supported by the XRD results which show peak broadening for samples annealed below 600 °C. The crystallite dimensions in terms of aspect ratio (length over diameter) are given in Table 4. Values close to one mean that the morphology approaches the spherical shape. It is also observed that the crystallites of the Cu doped samples are comparatively well-formed. The crystallite size of the $Zn_{0.99}Cu_{0.01}O$ materials is also larger in comparison to the ZnO materials at the same annealing conditions. It is evident here that morphology and size of crystallites influence the cell parameters of materials.

Fig. 6 shows TEM images of the samples Z400 and ZC400. The higher resolution images clearly show that the crystallites have nano scale dimensions for both samples and supports the SEM results given in Figs. 3(a) and 4(a) and dimensional values as listed

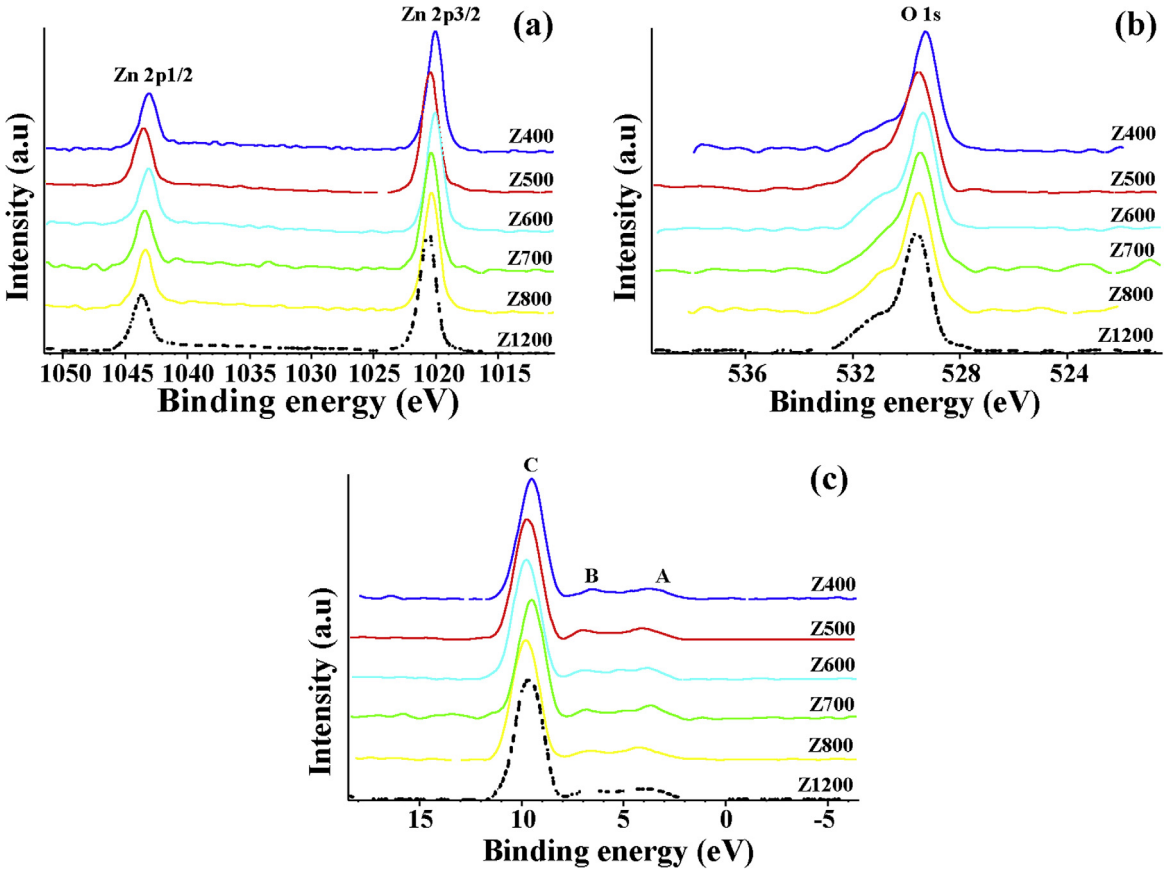

Fig. 13. XPS spectra for ZnO (a) Zn2p (b) O 1s and (c) valence band.

in Table 4. This proves that the materials are nanostructured in nature.

Band gaps are evaluated from the absorption edges of the reflectance spectra as shown in Figs. 7 and 8 for ZnO and $Zn_{0.99}Cu_{0.01}O$ materials respectively. The Tauc plots for ZnO and $Zn_{0.99}Cu_{0.01}O$ materials are shown in Figs. 9 and 10 respectively. The well known Tauc equation, Eq. (1), below is used,

$$(\alpha h\upsilon)^2 = C'(h\upsilon - Eg) \quad (1)$$

where α is the absorption coefficient of the material, λ is the wavelength, h is Planck's constant, C' is the proportionality constant, υ is the frequency of light and Eg is the band gap energy [2,41]. The graph plotted is $(\alpha h\upsilon)^2$ vs $h\upsilon$ and from Eq. (1), extrapolating the linear part of the graph until it meets the x-axis will give the value of the band gap [2] and results are shown in Figs. 9 and 10. The band gap energies of the materials are listed in Table 5. It is observed that the band gap energies increase with the reduction in crystallite size for both pure ZnO and Cu doped ZnO materials. The effect of the nano crystals is the widening of the band gap of the materials and agrees with earlier published work [2,42–44]. The band gap widening can be said to be attributable to the internal stress of the nano crystals and not due to quantum confinement effects because the crystallite size is much larger than the exciton Bohr radius [45]. It is also observed that upon Cu doping, the band gap narrows with respect to the pure ZnO materials. The observed narrowing of the band gap in Cu doped ZnO materials is believed to be due to the increased hybridization of the energy levels by the presence of the 3d transition metal, Cu, shifting the valence and conduction bands and subsequently decreasing the band gap. Narrowing of the band gap of the Cu doped materials is further investigated using XPS as is discussed below.

The narrowing of the band gap is attributed to the influence of the Cu^{2+} ions in the crystal lattice. It is known that the band gap of CuO is smaller than the band gap of ZnO (band gap of ZnO = 3.37 eV [46] and band gap of CuO = 1.2–1.3 eV [47]), thus, the Cu^{2+} ions have modified the band structure of the ZnO material.

In order to further understand the effect of spatial dimensions of the crystallites on the band gap, graphs of band gap versus diameter and length of the ZnO nanorods are shown in Fig. 11(a) and (b) respectively. For the more spherically shaped $Zn_{0.99}Cu_{0.01}O$ material, a graph of band gap against average diameter is shown in Fig. 12. The graphs show the band gap widening of the nanomaterials where the change is largest between 40 and 800 nm length scales. This demonstrates that the band gap change is most affected when the crystallite size is small.

It can be seen from the shifting of the absorption edge of ZnO and $Zn_{0.99}Cu_{0.01}O$ nano materials that the fundamental property of band gap of nanomaterials are different from the micron sized materials. Nanostructured materials have a smaller crystallite size with a shorter range order while larger micron sized crystallites have a longer range order implying that the number of atoms in the crystals can be very different.

To better understand the band gap widening and narrowing, further investigations using XPS on the materials are done. The XPS core level spectra for ZnO and $Zn_{0.99}Cu_{0.01}O$ materials are shown in Figs. 13 and 14 respectively while the binding energies (B.E.) are listed in Tables 6 and 7 for ZnO and $Zn_{0.99}Cu_{0.01}O$ materials respectively. All the binding energies are corrected using the C 1s peak (using the JEOL reference of C 1s B.E. = 284.2 eV) as a Ref. [48] and a Shirley background was used in the peak fitting. The oxidation states of Cu were determined by deconvolution of the asymmetric peaks and Fig. 15 is a representation of the results for samples ZC400 and ZC1200 (similarly for the other samples

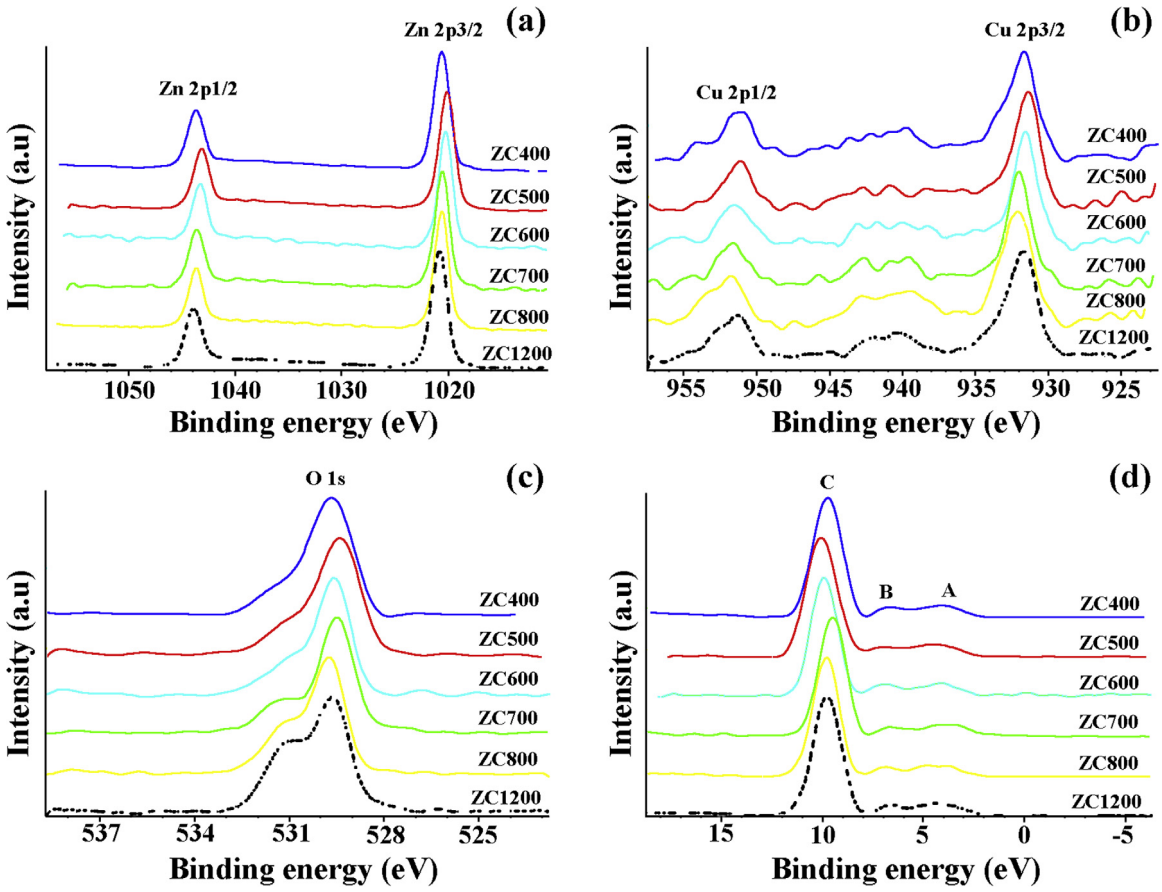

Fig. 14. XPS spectra for $Zn_{0.99}Cu_{0.01}O$ materials for (a) Zn2p (b) Cu2p (c) O 1s and (d) valence band.

Table 6
XPS binding energies of ZnO samples annealed at different temperatures.

Samples	Component	B.E (eV)	%	
			O 1	O 2
Z400	$Zn2p_{3/2}$	1020.17		
	$Zn2p_{1/2}$	1043.24		
	O1s	529.36	76.57	23.43
		530.976		
Z500	$Zn2p_{3/2}$	1020.53		
	$Zn2p_{1/2}$	1043.61		
	O1s	529.508	58.28	41.72
		530.835		
Z600	$Zn2p_{3/2}$	1020.13		
	$Zn2p_{1/2}$	1043.22		
	O1s	529.387	64.80	35.20
		530.832		
Z700	$Zn2p_{3/2}$	1020.44		
	$Zn2p_{1/2}$	1043.55		
	O1s	529.470	74.71	25.29
		530.774		
Z800	$Zn2p_{3/2}$	1020.41		
	$Zn2p_{1/2}$	1043.5		
	O1s	529.558	67.98	32.01
		531.06		
Z1200	$Zn2p_{3/2}$	1020.65		
	$Zn2p_{1/2}$	1043.75		
	O1s	529.605	64.90	35.10
		531.107		

as well (not shown)). For both groups of materials (ZnO and $Zn_{0.99}Cu_{0.01}O$), it is observed that the Zn2p core level doublets due to the spin–orbit coupling are typical of ZnO materials in terms of binding energy, peak shape and peak separation which is 23 eV [49–51]. The ratio of the $2p_{1/2}$ to $2p_{3/2}$ agrees well with the 1:2 ratio of the doublets for ZnO material as obtained by analysis of integrated peak intensities. The ratio for $Cu2p_{1/2}$ to $2p_{3/2}$ also agrees well with the published literature for CuO material. For the $Zn_{0.99}Cu_{0.01}O$ material, due to the asymmetric peak shape, indications are that both Cu^{+} and Cu^{2+} ions are present in the sample and this is especially obvious for the XPS results of the ZC400 sample which shows a shoulder in the $Cu2p_{3/2}$ peak. In addition, as shown in Fig. 14(b), satellite peaks, about 9 eV higher than the main $2p_{3/2}$ peak, are observed for all the doped samples and this is a clear indication of the presence of Cu^{2+} in the samples [29,52]. The satellite peak is due to the shake-up peak of the Cu^{2+} ions. Shake-up peaks occur in the Cu^{2+} ions because of the d^9 electronic configuration of the Cu^{2+} [53]. The satellite peak is actually due to the outgoing electron interacting with the unpaired d electron which "shakes it up", losing some of its kinetic energy [53–55] and as a result, a higher binding energy peak appears in the spectra. That is why this satellite peak is also often referred to as a shake up peak. In the measurement process, this will register readings of a higher binding energy than the main line as observed in the results of Fig. 14(b). The satellite peak is not observed for Cu_2O because the Cu exists in the Cu^{+} state. The satellite peak is due to the unpaired electron in the d-orbitals of the Cu^{2+} ion [56,57]. For Cu in the +1 state, it has all the d-electrons fully paired as shown in Fig. 16 and it is stable, therefore it is difficult to excite the electrons in the d-orbital. In the Cu^{2+} state, there is one unpaired electron in the orbital and this electron can easily interact with an out-going electron, absorbing an amount of energy and excited to a higher energy level. The out-going electron will thus have a lower energy and when it is detected by the XPS

Table 7
XPS analysis of $Zn_{0.99}Cu_{0.01}O$ samples annealed at different temperatures.

Samples	Component	B.E (eV)	%		%	
			Cu^+	Cu^{2+}	O 1	O 2
ZC400	$Zn2p_{3/2}$	1020.47				
	$Zn2p_{1/2}$	1043.54				
	$Cu2p_{3/2}$	931.342	45.87	54.13		
		932.427				
	$Cu2p_{1/2}$	951.223				
	O1s	529.446			72.21	27.79
		530.887				
ZC500	$Zn2p_{3/2}$	1020.19				
	$Zn2p_{1/2}$	1043.31				
	$Cu2p_{3/2}$	931.078	42.33	57.67		
		932.011				
	$Cu2p_{1/2}$	951.124				
	O1s	529.356			67.84	32.16
		530.794				
ZC600	$Zn2p_{3/2}$	1020.33				
	$Zn2p_{1/2}$	1043.41				
	$Cu2p_{3/2}$	930.889	32.17	67.83		
		931.978				
	$Cu2p_{1/2}$	951.585				
	O1s	529.542			51.94	48.06
		530.682				
ZC700	$Zn2p_{3/2}$	1020.70				
	$Zn2p_{1/2}$	1043.81				
	$Cu2p_{3/2}$	931.124	13.68	86.32		
		932.232				
	$Cu2p_{1/2}$	951.673				
	O1s	529.567			74.47	25.53
		531.397				
ZC800	$Zn2p_{3/2}$	1020.69				
	$Zn2p_{1/2}$	1043.80				
	$Cu2p_{3/2}$	931.644	13.49	86.51		
		932.592				
	$Cu2p_{1/2}$	951.805				
	O1s	529.714			57.53	42.47
		531.072				
ZC1200	$Zn2p_{3/2}$	1020.85				
	$Zn2p_{1/2}$	1043.96				
	$Cu2p_{3/2}$	931.263	13.11	86.89		
		932.027				
	$Cu2p_{1/2}$	951.315				
	O1s	529.597			57.05	42.95
		531.105				

detector, a higher binding energy is registered. Thus, the satellite peak is only observed when there are Cu^{2+} ions in the material and it can be used as a measure of the amount of the Cu^{2+} in the material. It is observed that the peak shape of the satellite peaks is more prominent and distinctive for samples with higher annealing temperatures implying that the Cu^{2+} content has increased in these samples (600 °C and above). Deconvoluting the $Cu2p_{3/2}$ peak for Cu^+ and Cu^{2+} gives the quantification of the ions in the samples and confirms increased amounts of the Cu^{2+} ions in the samples annealed at higher temperatures as listed in Table 7. This result shows evidence of the important role of the Cu^{2+} ions in the band gap narrowing of the doped samples which also has important implications in the valence band studies discussed later.

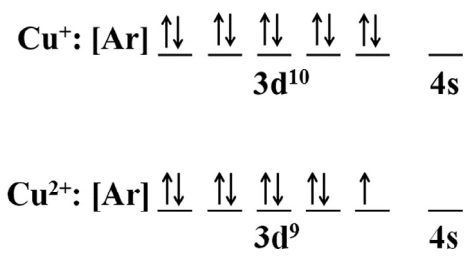

Fig. 16. The electronic configuration for Cu^+ and Cu^{2+} ions.

The oxygen 1 s core level peaks of the materials are shown in Figs. 13(b) and 14(c) for the ZnO and $Zn_{0.99}Cu_{0.01}O$ materials respectively. Two peaks are observed, with one main peak at a lower binding energy than the secondary peak. Deconvolution of the oxygen peaks are done as shown in Fig. 17(a) and (b) for samples ZC400 and ZC1200 (similarly for the other samples as well (not shown)). The main oxygen peak is attributed to the O^{2-} ions in the crystal lattice of the materials and our values (O binding energies) agree well with reported results for ZnO [36,51] and $Zn_{1-x}Cu_xO$ [58] materials (listed in Tables 6 and 7). In the ZnO materials, the peak shape and peak height of the secondary oxygen peak are similar for all samples and attributed to the surface adsorption of the hydroxyl, OH^- ions. We do not agree with the opinions of some researchers [35,36] that this may be due to oxygen vacancies because our quantitative XRD results do not show vacancies at the oxygen site in the crystal lattice of ZnO (for both micron and nanostructured ZnO). As explained above, since Zn has a high affinity to oxygen, then the likelihood of oxygen vacancies is small in ZnO. Furthermore, if there are oxygen vacancies, then these binding energies will not be detectable by the XPS. The B.E. of the secondary oxygen peak agrees well with the findings of Andersson [59,60] in his extensive doctoral research work and published paper on the hydroxyl adsorption on metal surfaces. Therefore, it is justifiable to attribute the higher B.E. oxygen to the hydroxyl that is attached to the surface of the ZnO and $Zn_{0.99}Cu_{0.01}O$ crystallites. It is, however, observed that the amount of hydroxyl in the $Zn_{0.99}Cu_{0.01}O$ materials increases with annealing

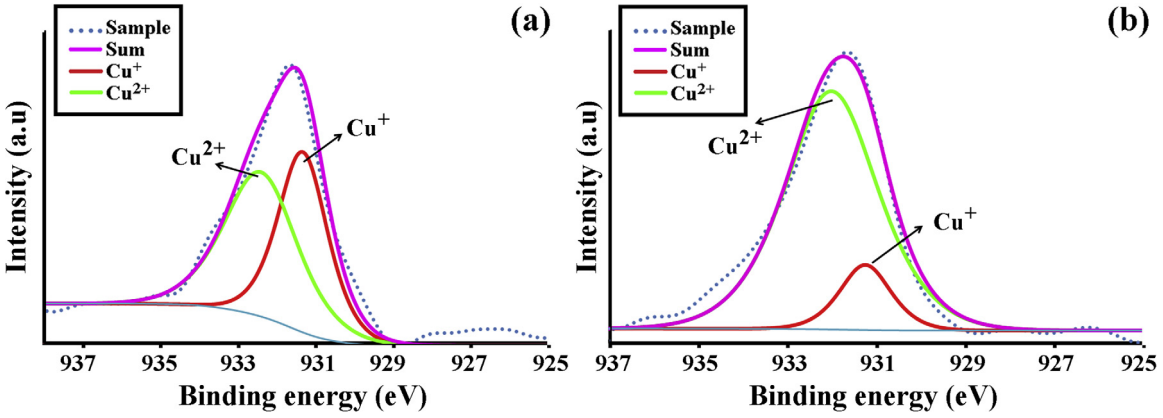

Fig. 15. The deconvolution of $Cu2p_{3/2}$ of (a) ZC400 and (b) ZC1200 sample.

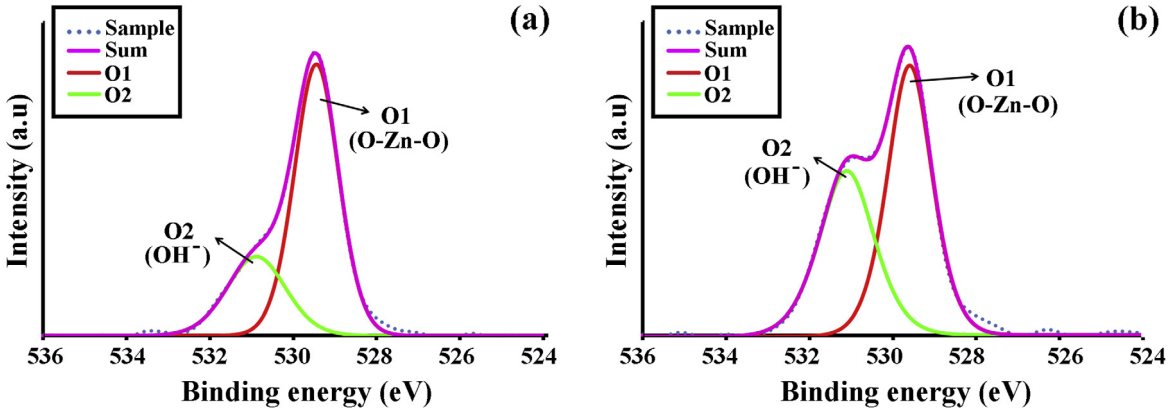

Fig. 17. The deconvolution of O 1s of (a) ZC400 and (b) ZC1200 sample.

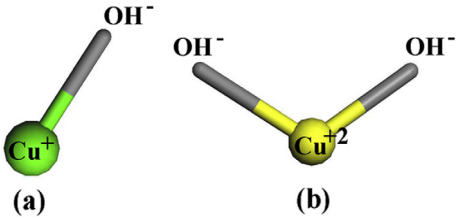

Fig. 18. The illustration of hydroxyl attachment to (a) Cu^{+} and (b) Cu^{+2}.

temperature (increase of about 33% in the ZC1200 with respect to ZC400 sample) as listed in Table 7. The increased OH^{-} in these samples can be explained by the increased Cu^{2+} content in the samples, particularly for the Cu^{2+} that resides at the surface of the crystallites. Cu^{+} can only attach one OH^{-} ion while Cu^{2+} on the surface can attach two OH^{-} ions as illustrated in the diagram of Fig. 18, thus, the increase of the secondary peak in the oxygen spectra of the Cu doped samples at higher annealing temperatures can be attributed to the increased hydroxyl adsorption on the surface of the particles. The XPS results of the increased Cu^{2+} amounts in the samples and the increased presence of the OH^{-} surface adsorption are proofs that the secondary O 1s peak is due to the adsorbed hydroxyls. Therefore, we have presented strong evidence that the higher B.E. oxygen can be attributed to the OH^{-} ions adsorbed on the surfaces of the crystallites.

Studies of valence band spectra of the materials are subsequently done to further understand the mechanisms of the band gap widening and narrowing of the materials. Valence band spectra of the ZnO and $Zn_{0.99}Cu_{0.01}O$ samples shown in Figs. 13(c) and 14(d) reveals three main peaks, A, B and C identified as valence, hybridized and d-orbital peaks respectively [61,62]. The valence band shifts of the nano and micron materials of ZnO and $Zn_{0.99}Cu_{0.01}O$ materials can be clearly seen in Fig. 19. In both cases, the shift is towards the higher binding energy values (to the left) implying that the valence band of nanomaterials is shifted downwards with respect to the highly crystalline materials. Fig. 20 shows a comparison of the valence band and conduction band positions for the nanostructured samples Z500 and ZC500 with their micron sized counterparts Z1200 and ZC1200 respectively. In both cases, at the nanoscale, it is observed that the valence band shifts downwards away from the conduction band for both pure ZnO and Cu doped ZnO with respect to the micron samples. The downward shift of the highest occupied molecular orbital (HOMO) of the valence band accounts for the band gap widening observed in nanomaterials because the degree of shift is greater than the conduction band shift. We have demonstrated here that it is possible to deduce the band energy shifts of the valence and conduction bands of the nanostructured materials with respect to the highly crystalline materials by employing the powerful XPS and UV–visible spectroscopic methods together. It is also observed that the shape of the A and B peaks for the ZnO nano and micron materials are different, that is, the peaks seem narrower for the nano ZnO and that there is also an increased separation of the peaks (marked by * in the diagram of Fig. 19(a)). Narrowing of the peak widths can be attributed to the decreased hybridization of energy levels in the nanomaterials as suggested earlier and this can also be an experimental proof of the increased discreteness of the energy

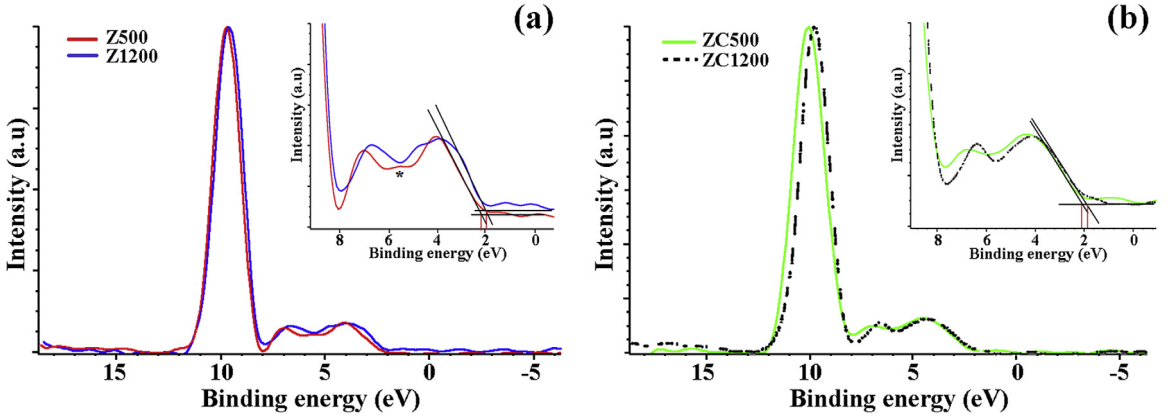

Fig. 19. Comparison of normalized VB XPS spectra of (a) Z500 and Z1200 (b) ZC500 and ZC1200 samples.

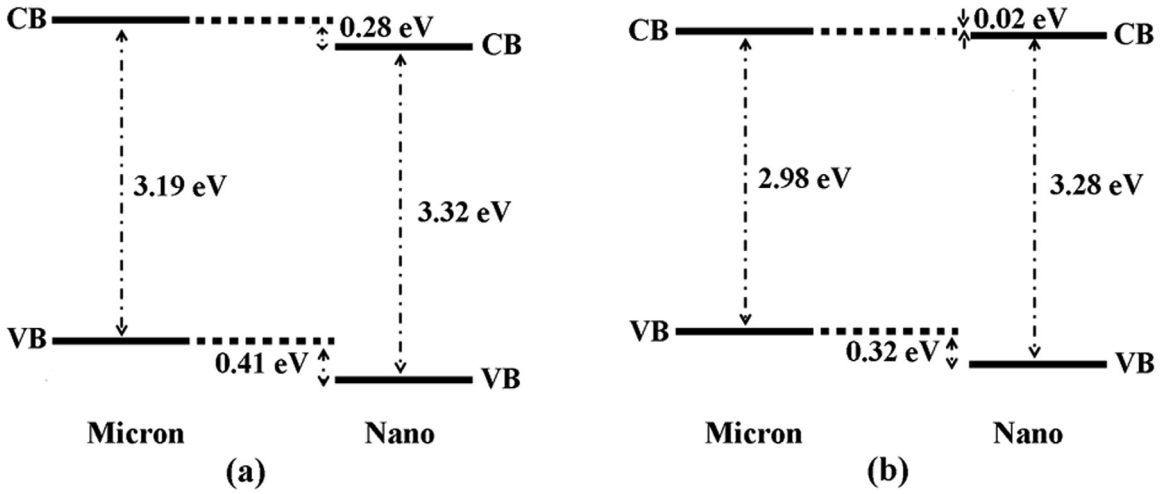

Fig. 20. The valence and conduction bands for nano and micron of (a) ZnO and (b) Cu doped ZnO samples.

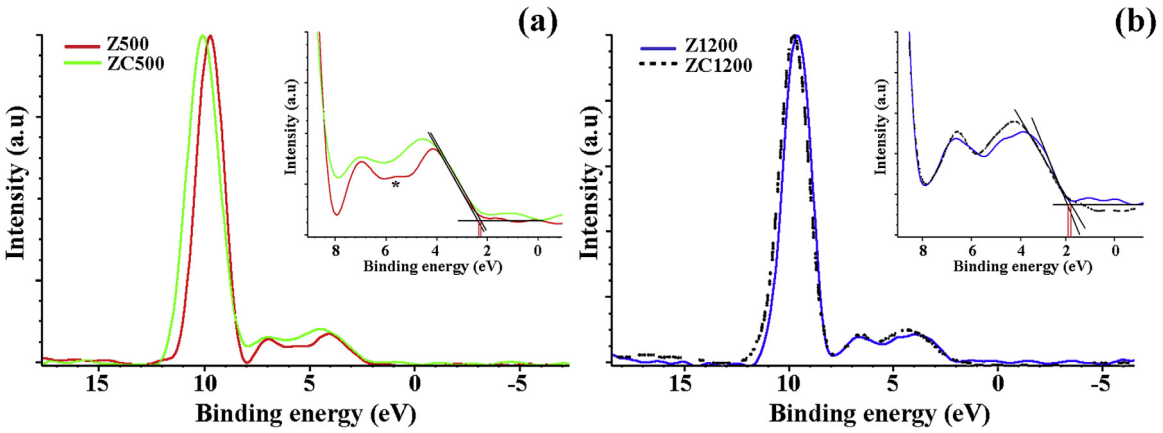

Fig. 21. Comparison of normalized VB XPS spectra of (a) Z500 and ZC500 (b) Z1200 and ZC1200 samples.

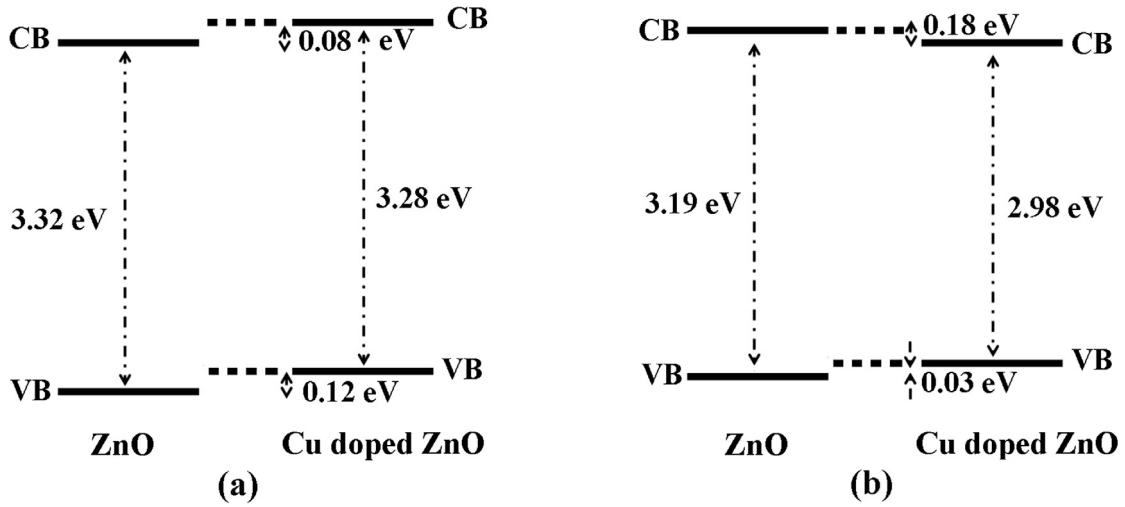

Fig. 22. The valence and conduction bands of undoped ZnO and Cu doped ZnO of (a) nano and (b) micron samples.

levels in the nanomaterials. The phenomenon is similarly observed in the Cu doped materials.

The undoped and Cu doped valence band spectra are compared to see the effects of doping at the nano as well as micro scales. XPS valence band spectra of the undoped and doped samples for nano and micron materials are shown in Fig. 21(a and b) respectively. It is observed that the valence band of the Cu doped materials is shifted to the right of the undoped valence band spectra for both nano and micron sized materials implying that the valence band maximum has shifted upwards with respect to the conduction

band of the doped compounds. Energy level diagrams of the ZnO and Cu doped ZnO for nano and micron samples are drawn to scale as shown in Fig. 22. It can be seen that for the nano materials (Fig. 22(a)), the top of the valence band (HOMO) of the Cu doped material is shifted upwards and the bottom of the conduction band, LUMO, is also shifted upwards with respect to the ZnO energy bands. For the micron sized materials, the VB maximum is shifted upwards but the CB minimum is shifted downwards. Therefore, the band gap narrowing of the Cu doped materials results in shifts of the VB and CB that is not identical for the nano and micron sized cases. Since the Cu^{2+} content is highest in the ZC1200 sample and the band gap is smallest for this sample, the narrowing of the band gap due to Cu doping is attributable to the Cu^{2+} ions instead of the Cu^{+} ions. This can be explained by the electron distribution in the d-orbitals of the Zn^{2+} and the Cu^{2+} ions which are different. The Zn^{2+} ions have complete pairings of electrons in their orbitals, $3d^{10}$, whereas in Cu^{2+}, the electronic orbital is $3d^{9}$. The presence of Cu^{2+} ions in the ZnO lattice is believed to have produced additional energy levels near and above the valence band of the ZnO, narrowing the band gap of the $Zn_{0.99}Cu_{0.01}O$ materials and accounting for the observed decrease in the band gap.

Conclusions

In conclusion, this work has demonstrated that the band gap widening of nanostructured ZnO and $Zn_{0.99}Cu_{0.01}O$ is due mainly to the downward shift of the valence band. It has also identified the reasons for the band gap narrowing of the Cu doped materials as due to the presence of the Cu^{2+} ions modifying the energy levels and narrowing the band gaps of the $Zn_{0.99}Cu_{0.01}O$ materials. Cu^{2+} ions with its unfilled 3d orbitals have shifted the valence band maximum upwards, narrowing the band gap. Thus, the mechanism for the band gap widening of nanomaterials for both ZnO and $Zn_{0.99}Cu_{0.01}O$, and the band gap narrowing of doped $Zn_{0.99}Cu_{0.01}O$ materials (with respect to pure ZnO) have been identified. The band gap narrowing for Cu doped materials is more pronounced in the highly crystalline materials than in the nano materials. Structural studies *via* quantitative XRD show that no oxygen vacancies are formed in the doped and undoped ZnO for all annealed samples showing the strong oxygen affinity of the material. No disorder of the ions is observed and no antisites are concluded to be present in the materials.

Author's contribution

N.K. is the project leader, conceived the ideas, and helped the research at every level inclusive of experimental, results, data interpretation and explanations, discussions and conclusion. M.F.K. carried out the synthesis and measurements of the characterization of the samples, and helped with the data analysis, preparation of results and manuscript. N.F.C. helped with the characterization and discussions of the samples using Transmission Electron Microscopy (TEM) and Scanning Electron Microscopy (SEM).

Acknowledgements

The authors would like to thank the Institute of Science, UiTM, for internal funding of the work.

References

[1] Anandan S, Ohashi N, Miyauchi N. ZnO-based visible-light photocatalyst: band gap engineering and multi electron reduction by co-catalyst. Appl Catal B 2011;210:18–22.
[2] Rusdi R, Rahman AA, Mohamed NS, Kamarudin N, Kamarulzaman N. Preparation and band gap energies of ZnO nanotubes, nanorods and spherical nanostructures. Powder Technol 2011;210:18–22.
[3] Carotta MC, Cervi A, Fioravanti A, Gherardi S, Giberti A, Vendemiati B, et al. A novel ozone detection at room temperature through UV-LED-assisted ZnO thick film sensors. Thin Solid Films 2011;520:939–46.
[4] Martinson ABF, Elam JW, Hupp JE, Pellin MJ. ZnO nanotube based dye-sensitized solar cells. Nano Lett 2007;7(8):2183–7.
[5] Kim DC, Han WS, Kong BH, Cho HK, Hong CH. Fabrication of the hybrid ZnO LED structure grown on p-type GaN by metal organic chemical vapor deposition. Phys B 2007;401–402:386–90.
[6] Snure M, Tiwari A. Band-gap engineering of $Zn_{1-x}Ga_xO$ nanopowders: synthesis, structural and optical characterizations. J Appl Phys 2008;104:073707.
[7] Zhang X, Qin J, Xue Y, Yu P, Zhang B, Wang L, et al. Effect of aspect ratio and surface defects on the photocatalytic activity of ZnO nanorods. Sci Rep 2014;4:04596.
[8] Marotti RE, Giorgi P, Machado G, Dalchiele EA. Crystallite size dependence of band gap energy for electrodeposited ZnO grown at different temperatures. Sol Energy Mater Sol Cells 2006;90:2356–61.
[9] Akhtar MS, Khan MA, Jeon MS, Yang OB. Controlled synthesis of various ZnO nanostructured materials by capping agents-assisted hydrothermal method for dye-sensitized solar cells. Electrochim Acta 2008;53:7869–74.
[10] Chayed NF, Badar N, Rusdi R, Azahidi A, Kamarulzaman N. Band gap energies of $Li_{2x}Mg_{(1-x)}O$ materials synthesized by the sol–gel method. J Cryst Growth 2013;362:268–70.
[11] Badar N, Kamarulzaman N, Rusdi R, Aziz NDA, Fun HK. Increased conductivities of Cr doped $Al_{2-x}Cr_xO_3$ powders due to band gap narrowing. Phys B 2014;437:32–5.
[12] Saleh R, Djaja NF. Transition-metal-doped ZnO nanoparticles: synthesis, characterization and photocatalytic activity under UV light. Spectrochim Acta A 2014;130:581–90.
[13] Coleman VA, Jagadish C. Zinc oxide bulk, thin films and nanostructures: basic properties and applications of ZnO. Elsevier Book; 2006. p. 1–20.
[14] Caglar M, Caglar Y, Aksoy S, Ilican S. Temperature dependence of d optical band gap & electrical conductivity of sol-gel derived undoped & Li-doped ZnO films. Appl Surf Sci 2010;256:4966–71.
[15] Shan FK, Liu GX, Lee WJ, Shin BC. Stokes shift, blue shift and red shift of ZnO-based thin films deposited by pulsed-laser deposition. J Cryst Growth 2006;291:328–33.
[16] Shan FK, Yu YS. Band gap energy of pure and Al-doped ZnO thin films. J Eur Ceram Soc 2004;24:1869–72.
[17] Salleh R, Prakoso SP, Fishli A. The influence of Fe doping on the structural, magnetic and optical properties of nanocrystalline ZnO particles. J Magn Magn Mater 2012;324:665–70.
[18] Chen Y, Xu XL, Zhang GH, Xue H, Ma SY. Blue shift of optical band gap in Er-doped ZnO thin films deposited by direct current reactive magnetron sputtering technique. Physica E 2010;42:1713–6.
[19] Liu H, Yang J, Hua Z, Zhang Y, Yang L, Xiao L, et al. The structure and magnetic properties of Cu-doped ZnO prepared by sol–gel method. Appl Surf Sci 2010;256:4162–5.
[20] Senthilkumaar S, Rajendran K, Banerjee S, Chini TK, Sengodan V. Influence of Mn doping on the microstructure and optical property of ZnO. Mater Sci Semicond Process 2008;11:6–12.
[21] Ahmad M, Ahmed E, Zhang Y, Khalid NR, Xu J, Ullah M, et al. Preparation of highly efficient Al-doped ZnO photocatalyst by combustion synthesis. Curr Appl Phys 2013;13:697–704.
[22] Lee JH, Park BO. Characteristics of Al-doped ZnO thin films obtained by ultrasonic spray pyrolysis: effects of Al doping and an annealing treatment. Mater Sci Eng B 2004;106:242–5.
[23] Chao CH, Han CH, Huang JJ, Chang LS, Shih HC. Manipulated the band gap of 1D ZnO nano-rods array with controlled solution concentration and its application for DSSCs. Curr Appl Phys 2011;11:S136–9.
[24] Thilagavathi T, Geetha D. Nano ZnO structures synthesized in presence of anionic and cationic surfactant under hydrothermal process. Appl Nanosci 2014;4:127–32.
[25] Yan X, Itoh T, Dai S, Ozaki Y, Fang Y. Cu, Mn doping effect to optical behavior and electronic structure of ZnO ceramic. J Phys Chem Solids 2013;74:1127–30.
[26] Wang DF, Zhang TJ. Study on the defects of ZnO nanowire. Solid State Commun 2009;149:1947–9.
[27] Leung YH, Chen XY, Ng AMC, Guo MY, Liu FZ, Djurisic AB, et al. Green emission in ZnO nanostructures—Examination of the roles of oxygen and zinc vacancies. Appl Surf Sci 2013;271:202–9.
[28] Chow L, Lupan O, Chai G, Khallaf H, Ono LK, Roldan Cuenya B, et al. Synthesis and characterization of Cu doped ZnO one-dimensional structures for miniaturized sensor applications with faster response. Sen Actuators A 2013;189:399–408.
[29] Xue H, Chen Y, Xu XL, Zhang GH, Zhang H, Ma SY. X-ray diffraction spectroscopy and X-ray photoelectron spectroscopy studies of Cu-doped ZnO films. Physica E 2009;41:788–91.
[30] Caglar M, Yakuphanoglu F. Structural and optical properties of copper doped ZnO films derived by sol–gel. Appl Surf Sci 2012;258:3039–44.
[31] Jongnavakit P, Amornpitoksuk P, Suwanboon S, Ndiege N. Preparation and photocatalytic activity of Cu-doped ZnO thin films prepared by the sol–gel method. Appl Surf Sci 2012;258:8192–8.
[32] David WI F, Shankland K, McCusker LB, Baerlocher Ch. Structure determination from powder diffraction data. Oxford University Press; 2002.
[33] Zenkins R, Snyder RL. Introduction to X-Ray powder diffractometry. New York: John Wiley and Sons, INC; 1996.

[34] Pecharsky VK, Zavalij PY. Fundamentals of powder diffraction and structural characterization of materials. Springer; 2005.
[35] Ansari SA, Khan MM, Kalathil S, Nisar A, Lee J, Cho MH. Oxygen vacancy induced band gap narrowing of ZnO nanostructures by an electrochemically active biofilm. Nanoscale 2013;5:9238–46.
[36] Wang J, Wang Z, Huang B, Ma Y, Liu Y, Qin X, et al. Oxygen vacancy induced band-gap narrowing and enhanced visible light photocatalytic activity of ZnO. ACS Appl Mater Interfaces 2012;4:4024–30.
[37] Janotti A, Van de Walle CG. New insights into the role of native point defects in ZnO. J Cryst Growth 2006;287:58–65.
[38] Mary JA, Vijaya JJ, Bououdina M, Kennedy LJ, Daie JH, Song Y. Investigation of structural, surface morphological, optical properties and first-principles study on electronic and magnetic properties of (Ce, Fe)-codoped ZnO. Phys B 2015;456:344–54.
[39] Zhao Z, Song J, Zheng J, Lian J. Optical properties and photocatalytic activity of Nd-doped ZnO powders. Trans Nonferrous Met Soc China 2014;24:1434–1439.
[40] Lide David R. Handbook of chemistry and physics. 76th ed. CRC Press, INC; 1995–1996.
[41] Pearton SJ, Norton DP, Ip K, Heo YW, Steiner T. Recent progress in processing and properties of ZnO. Prog Mater Sci 2005;50:293–340.
[42] Sahu SN, Nanda KK. Nanostructure semiconductors: physics and applications. PINSA 2001;67(A):103–30.
[43] Makkar M, Bhatti HS. Inquisition of reaction parameters on the growth and optical properties of ZnO nanoparticles synthesized via low temperature reaction route. Chem Phys Lett 2011;507:122–7.
[44] Singla ML, Muhamed Shafeeq M, Kumar M. Optical characterization of ZnO nanoparticles capped with various surfactants. J Lumin 2009;129:434–438.
[45] Chandrasekaran P, Viruthagiri G, Srinivasan N. The effect of various capping agents on the surface modifications of sol-gel synthesized ZnO nanoparticles. J Alloys Compd 2012;540:89–93.
[46] Murugadoss G. Synthesis and characterization of transition metals doped ZnO nanorods. J Mater Sci Technol 2012;28(7):587–93.
[47] Johan MR, Mohd Suan MS, Hawari NL, Ching HA. Annealing effects on the properties of copper oxide thin films prepared by chemical deposition. Int J Electrochem Sci 2011;6:6094–104.
[48] Ikeo N, Iijima Y, Niimura N, Sigematsu M, Tazawa T, Matsumoto S, et al. Handbook of X-ray photoelectron spectroscopy, 1991.
[49] Hu D, Liu X, Deng S, Liu Y, Feng Z, Han B, et al. Structural and optical properties of Mn-doped ZnO nanocrystalline thin films with the different dopant concentrations. Physica E 2014;61:14–22.
[50] Wagner CD, Naumkin AV, Kraut-Vass A, Allison JW, Powell CJ, Rum-ble Jr JR. NIST Standard Reference Database 20, Version 3.4 (web version) (http://srdata.nist.gov/xps/), 2003.
[51] Al-Gaashani R, Radiman S, Daud AR, Tabet N, Al-Douri Y. XPS and optical studies of different morphologies prepared by microwave methods. Ceram Int 2013;39:2283–92.
[52] Biesinger MC, Payne BP, Hart BR, Grosvenor AP, McIntryre NS, Lau LWM, et al. Quantitative chemical state XPS analysis of first row transition metals, oxides and hydroxides. J Phys 2008;100:012025.
[53] Hüfner S. Photoelectron spectroscopy: principles and applications. Springer; 2003.
[54] Van der Heide PAW. Multiplet splitting patterns exhibited by the first row transition metal oxides in X-ray photoelectron spectroscopy. J Electron Spectrosc 2008;164:8–18.
[55] Svintsitsky DA, Chupakhin AP, Slavinskaya EM, Stonkus OA, Stadnichenko AI, Koscheev SV, et al. Study of cupric oxide nanopowders as efficient catalyst for low-temperature CO oxidation. J Mol Catal A 2013;368–369:95–106.
[56] Biesinger Mark C, Lau Leo WM, Gerson Andrea R, Smart Roger StC. Resolving surface chemical states in XPS analysis of first row transition metals, oxides and hydroxides: Sc, Ti, V, Cu and Zn. Appl Surf Sci 2010;257:887–98.
[57] Ghodselahi T, Vesaghi MA, Shafiekhani A, Baghizadeh A, Lameii M. XPS study of the Cu @ Cu2O core-shell nanoparticles. Appl Surf Sci 2008;255:2730–4.
[58] Li FM, Zhu CT, Ma SY, Sun AM, Song HS, Li XB, et al. Investigation of the blue–green emission and UV photosensitivity of Cu-doped ZnO films. Mat Sci Semicon Proc 2013;16:1079–85.
[59] Andersson K. Structure, bonding and chemistry of water and hydroxyl on transition metal surfaces. Stockholm University; 2006.
[60] Schiros T, Naslund LA, Anderson K, Gyllenpalm J, Karlberg GS, Odelius M, et al. Structure and bonding of the water-hydroxyl mixed phase on Pt(111). J Phys Chem C 2007;111:15003–12.
[61] Gabas M, Gota S, Ramos-Barrado JR, Barret NT, Avilla J, Sacchi M. Unraveling the conduction mechanism of Al-doped ZnO films by valence band soft X-ray photoemission spectroscopy. Appl Phys Lett 2005;86:042104.
[62] Cong GW, Peng WQ, Wei HY, Han XX, Wu JJ, Liu XL, et al. Comparison of valence band X-ray photoelectron spectrum between Al-N-codoped and N-doped ZnO films. Appl Phys Lett 2006;88:062110.